

# Digital Control System for the MEMS Tuning Fork Gyroscope Based on Synchronous Integral Demodulator

Cheng Yang and Hongsheng Li

**Abstract**—This paper presents a demodulation algorithm based on the synchronous integrator circuit for the MEMS tuning fork gyroscope utilizing the digital processing technology. The synchronous integral demodulator (SID) is adopted to demodulate the drive-detection signal and sense-axis output signal separately. Combining with automatic gain control and phase-locked loop technology, the closed-loop control of drive mode has been implemented, and high precision output of the gyroscope has been achieved. The simulation results have verified the effectiveness of the synchronous integrator circuit, which is in good agreement with the theoretical analysis. Compared with other demodulation algorithms, the SID has the advantages of the lower noise level, a better ability to attenuate the harmonics, and the best hardware efficiency. The frequency characteristic of the synchronous integrator is also analyzed, which is vital to the bandwidth of gyroscope. The print circuit board based on field-programmable gate array digital circuit is manufactured and the corresponding experiment is carried out. The experimental results show that the SID algorithm of digital control system for the gyroscope developed in our laboratory has achieved a good performance. The bias instability of tested gyroscope is measured to be  $0.2^\circ/\text{h}$  with the angle random walk of  $0.14^\circ/\sqrt{\text{h}}$  and the nonlinearity of the scale factor is  $<60$  ppm with the measurement range of  $\pm 100^\circ/\text{s}$ .

**Index Terms**—Demodulation algorithm, digital control system, micro electro mechanical system (MEMS), synchronous integrator, tuning fork gyroscope.

## I. INTRODUCTION

MEMS gyroscopes have achieved rapid development in recent years; it has many advantages over traditional gyroscopes for low cost, low power consumption, small size and excellent shock survival capability. They have been widely applied in commercial and military fields, such as angular velocity measurement systems, consumer electronics, automotive safety systems, robot control systems and micro inertial measurement unit navigation systems [1]. Some micro-gyroscopes have reached the required tactical grade [2]–[5],

Manuscript received June 9, 2015; accepted June 24, 2015. Date of publication June 30, 2015; date of current version August 14, 2015. This work was supported in part by the Pre-Research Fund Project under Grant 9140A09011313JW06119 and in part by the Jiangsu Provincial Key Technology Research and Development Program under Grant BE2014003-3. The associate editor coordinating the review of this paper and approving it for publication was Prof. Weileun Fang.

The authors are with the Key Laboratory of Micro-Inertial Instrument and Advanced Navigation Technology, School of Instrument Science and Engineering, Ministry of Education, Southeast University, Nanjing 210096, China (e-mail: ycb\_ye@163.com; hsl@seu.edu.cn).

Color versions of one or more of the figures in this paper are available online at <http://ieeexplore.ieee.org>.

Digital Object Identifier 10.1109/JSEN.2015.2451080

and inertial grade [6]. Due to inferior processing technology, the performance of Micro Electro Mechanical System (MEMS) gyroscope developed in China has a big gap with that of products. Measuring circuits, demodulation algorithms and control strategies should be considered to improve the precision of MEMS gyroscopes under the current processing technology.

The traditional analog readout systems suffer from temperature drift and difficulties for realizing the complex algorithm. In contrast, the digital readout systems have the advantages of flexibility and insensitivity to environmental parameters; hence, currently the digital readout systems of micro-gyroscope have been widely applied [7]–[9]. In digital controllers, quadrature demodulation is preferred as it can obtain the amplitude and phase of the output signal of gyroscope simultaneously [10]. Multiplication demodulator [11] and least mean square (LMS) demodulator [12]–[14] are commonly used as demodulation algorithms in digital control systems. Multiplication demodulator (MD) is a very popular algorithm which contains a multiplier and a low-pass filter, yet it exhibits poor performances of noise immunity and harmonics suppression. Due to multiplying, the demodulator will generate a second harmonic component, which cannot be completely eliminated by a low-pass filter. The response time, bandwidth and noise level are also limited by the filter. LMS demodulator (LMSD) is an adaptive algorithm, which is known for its low computational complexity and robustness in different running environments, making the reference signal fast converge to the input signal. The LMS adaptive filter consists of two orthogonal one-order filters, and the coefficients are the demodulation results which can be obtained by sufficient iterations. However, the choice of convergence factor has a complex impact on the stability and start-up time of the algorithm. In addition, in [15], the authors introduced a Fourier demodulation algorithm, whose noise immunity is stronger than that of the MD. However, the algorithm requires at least one sampling period and different cycles with the same sampling phases to obtain the demodulated output data. Fourier demodulator (FD) is quite sophisticated and costs much more logic resources. Synchronous integrator, which was first presented in 1965 [16], is an effective method to extract the sinusoidal signal or square wave signal from the noise. Applying the technique to MEMS gyroscopes as a demodulator has not been mentioned in previous literatures.

For the decoupled dual-mass MEMS tuning fork gyroscope developed at Southeast University, this paper presents

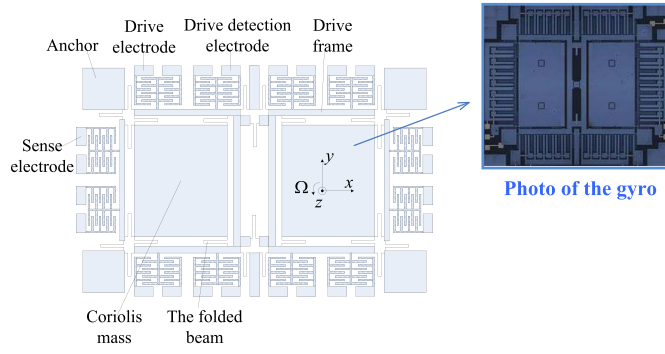


Fig. 1. Simplified schematic of the MEMS tuning fork gyroscope.

a demodulation algorithm based on the synchronous integrator circuit. The digital control system for the gyroscope has been established, wherein, most of the control algorithm is implemented in FPGA platform.

This paper is organized as follows. Section II introduces the basic model of the MEMS tuning fork gyroscope developed in our laboratory. The basic principle of synchronous integrator detection technology is analyzed in Section III. The equations of amplitude and phase obtained by synchronous integrator are also deduced. In Section IV, the frequency characteristic of synchronous integrator is analyzed, which is vital to the bandwidth of gyroscope system. Section V shows the simulations and analyses of the synchronous integrator; the results verify the theoretical analyses carried out in the former sections. Several demodulation algorithms are also simulated to compare their performances. Section VI gives the digital control system for the MEMS tuning fork gyroscope. In order to verify the feasibility of synchronous integrator demodulation algorithm, the gyroscope control circuit is designed and relevant tests are carried out in Section VII. At last, Section VIII concludes this paper.

## II. BASIC MODEL OF MEMS TUNING FORK GYROSCOPE

The MEMS gyroscope researched in our laboratory [17] is a conventional silicon tuning fork Coriolis Vibratory Gyro (CVG) type, as shown in fig. 1, which has the form of dual-mass and full-decoupled. The design of dual-mass structure can realize the difference detection of the Coriolis acceleration and suppress the common mode interference. The folded beams are adopted to reduce the mechanical coupling between the driving mode and sense mode. Driving voltage, an AC voltage biased by a DC potential, applied to the drive electrodes excites the proof masses into resonance along the x-axis; According to the Coriolis effect, when the gyroscope rotates around the z-axis, the induced Coriolis force will drive the proof masses to vibrate in the y-axis. The vibration signal detected by the sense electrodes is processed to obtain the input angular rate  $\Omega_z$ .

The drive mode and sense mode of MEMS tuning fork gyroscope can be considered as two “mass-spring-damper” second-order vibration systems. As to the structure-decoupled

micro-gyroscope, its ideal kinetic equation can be described as:

$$\begin{bmatrix} m_x & 0 \\ 0 & m_y \end{bmatrix} \begin{bmatrix} \ddot{x} \\ \ddot{y} \end{bmatrix} + \begin{bmatrix} c_x & 0 \\ 0 & c_y \end{bmatrix} \begin{bmatrix} \dot{x} \\ \dot{y} \end{bmatrix} + \begin{bmatrix} k_x & 0 \\ 0 & k_y \end{bmatrix} \begin{bmatrix} x \\ y \end{bmatrix} = \begin{bmatrix} F_e \\ -2m_y\Omega_z\dot{x} \end{bmatrix} \quad (1)$$

where  $x$  and  $y$  are the displacements of drive mode and sense mode,  $m_x$  and  $m_y$  are the masses in x-axis direction and y-axis direction;  $c_x$  and  $c_y$  represent the damp coefficients in each mode,  $k_x$  and  $k_y$  are the spring coefficients in each mode.  $F_e$  is the external force applied to drive mode.  $\Omega_z$  is the input angular rate with respect to z-axis.

Assume that the driving force  $F_e$  is  $F_d \sin(\omega_d t)$  and the frequency of driving force is equal to the natural frequency of the drive mode, i.e.  $\omega_d = \omega_{nx}$ , which can be guaranteed by the drive control loop. The displacement in the x-axis direction and the y-axis direction can be represented by:

$$\begin{cases} x(t) = \frac{F_d Q_x}{m_x \omega_d^2} \sin(\omega_d t - \frac{\pi}{2}) \\ y(t) = \frac{-2\Omega_z \omega_d A_x}{\sqrt{(\omega_{ny}^2 - \omega_d^2)^2 + \omega_{ny}^2 \omega_d^2 / Q_y^2}} \sin(\omega_d t + \theta_y) \end{cases} \quad (2)$$

where  $A_x = F_d Q_x / m_x \omega_d^2$  is the displacement amplitude of drive direction,  $\omega_{nx} = \sqrt{k_x / m_x}$  and  $\omega_{ny} = \sqrt{k_y / m_y}$  are the natural frequency of the drive mode and sense mode, respectively.  $Q_x = m_x \omega_{nx} / c_x$  and  $Q_y = m_y \omega_{ny} / c_y$  are the quality factor in each mode.  $\theta_y = -\tan^{-1}(\frac{\omega_{ny} \omega_d}{(\omega_{ny}^2 - \omega_d^2) Q_y})$  is the phase delay of sense mode.

The mechanical sensitivity of MEMS tuning fork gyroscope can be represented by:

$$S = \frac{|y(t)|}{\Omega_z} = \frac{2\omega_d A_x}{\sqrt{(\omega_{ny}^2 - \omega_d^2)^2 + \omega_{ny}^2 \omega_d^2 / Q_y^2}} \quad (3)$$

Equation (3) can be further simplified as [18]:

$$S \approx \frac{A_x}{|\omega_{ny} - \omega_d|} \quad (4)$$

From (4), it can be observed that the mechanical sensitivity is mainly determined by the frequency difference between the drive and sense mode and the displacement amplitude of drive mode. In order to get accurate information of input angular rate, the drive loop must track the gyroscope resonant frequency and maintain the drive amplitude stably by adopting closed-loop control.

In addition to the mechanical sensitivity, bandwidth is also an important parameter of the micro-gyroscope. The open-loop bandwidth of gyroscope can be determined by [19]:

$$BW = 0.54 |\omega_{ny} - \omega_d|. \quad (5)$$

## III. SYNCHRONOUS INTEGRATOR DETECTION TECHNOLOGY

Synchronous integrator [16] is controlled by synchronous switches so that capacitors are charged by in-phase signals with the same frequency. The potential value of the capacitor is the integral value of signal within the charging time. Since the

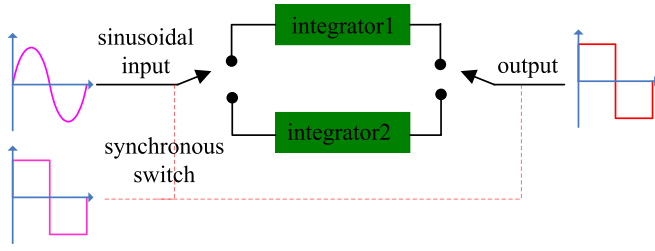


Fig. 2. The schematic of synchronous integrator.

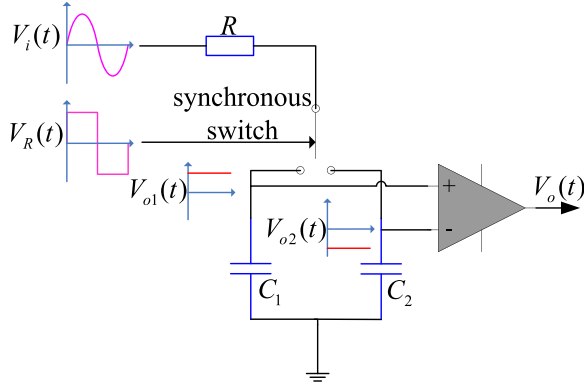


Fig. 3. The first-order synchronous integrator circuit.

random noise cannot be synchronized with the control switch, it will be suppressed by charging capacitor. Therefore, the useful signal can be extracted from the noise and interference signals in this way. The synchronous integrator can be viewed as a square-wave matched filter whose band-pass frequency can be determined by control signals of the switches.

The schematic of synchronous integrator is shown in fig. 2. Sinusoidal wave or square wave has only two states in a cycle: positive output with a phase of naught to 180 degrees and negative with 180 to 360 degrees. By only two integrators, the input signal is synchronized to the integrator, and meanwhile the output load is connected to the integrator by synchronous switch respectively. When the input signal is in the positive half cycle, synchronous switch is connected to the input and output via the integrator 1; conversely, when the input signal is in the negative half cycle, synchronous switch is connected to the input and output via the integrator 2.

Fig.3 shows the basic circuit of the first-order synchronous integrator. Assume that the synchronous control signal is a square wave with unit amplitude. When the synchronous signal is in a logic high state, the electronic switch is connected to the capacitor  $C_1$ ; when the synchronous signal is in a logic low state, the switch is connected to the capacitor  $C_2$ . The Fourier expansion of the square wave with a frequency of  $\omega_R$  can be written as:

$$V_R = \frac{4}{\pi} \sum_{n=0}^{\infty} \frac{1}{2n+1} \sin(2n+1)\omega_R t \quad (6)$$

Assume the input signal is  $V_i = V_m \sin(\omega t + \varphi)$ . As the capacitor  $C_1$  and  $C_2$  are respectively connected to  $R$ , the equivalent integrator circuit can be described as the following

differential equations:

$$\begin{cases} \frac{dV_{o1}}{dt} + \frac{1}{R_1 C_1} V_{o1} = \frac{1}{R_1 C_1} V_{i1} \\ \frac{dV_{o2}}{dt} + \frac{1}{R_2 C_2} V_{o2} = \frac{1}{R_2 C_2} V_{i2} \end{cases} \quad (7)$$

where  $V_{i1} = (1 + V_R) \cdot V_i / 2$  and  $R_1 = 2R / (1 + V_R)$  represent equivalent input voltage and resistance when the capacitor  $C_1$  is connected to  $R$ , respectively;  $V_{i2} = (1 - V_R) \cdot V_i / 2$  and  $R_2 = 2R / (1 - V_R)$  are equivalent input voltage and resistance when the capacitor  $C_2$  is connected.

If the conditions of  $2RC_1\omega \gg 1$ ,  $2RC_2\omega \gg 1$  are met, the above equations can be solved as:

$$\begin{cases} V_{o1}(\omega) = \frac{2V_m}{\pi} \sum_{n=0}^{\infty} \frac{1}{2n+1} \left( \frac{\cos((\omega - (2n+1)\omega_R)t + \varphi + \theta_1)}{\sqrt{1 + (2RC_1(\omega - (2n+1)\omega_R))^2}} - e^{-\frac{t}{2RC_1}} \frac{\cos(\varphi + \theta_1)}{\sqrt{1 + (2RC_1(\omega - (2n+1)\omega_R))^2}} \right) \\ V_{o2}(\omega) = -\frac{2V_m}{\pi} \sum_{n=0}^{\infty} \frac{1}{2n+1} \left( \frac{\cos((\omega - (2n+1)\omega_R)t + \varphi + \theta_2)}{\sqrt{1 + (2RC_2(\omega - (2n+1)\omega_R))^2}} - e^{-\frac{t}{2RC_2}} \frac{\cos(\varphi + \theta_2)}{\sqrt{1 + (2RC_2(\omega - (2n+1)\omega_R))^2}} \right) \end{cases} \quad (8)$$

$$\begin{cases} \theta_1(\omega) = \arctg(2RC_1(\omega - (2n+1)\omega_R)) \\ \theta_2(\omega) = \arctg(2RC_2(\omega - (2n+1)\omega_R)) \end{cases} \quad (9)$$

Generally  $C_1 = C_2 = C$ , the output voltage of the synchronous integrator can be written as:

$$V_o = V_{o1} \cdot V_R \quad (10)$$

When the frequency of switching signal is the same as the input signal, which means  $\omega = \omega_R$ , the output of synchronous integrator can be expressed as:

$$V_{o1} = \frac{2V_m}{\pi} (1 - e^{-\frac{t}{2RC}}) \cos \varphi \quad (11)$$

Considering  $t \gg 2RC$ , it will have the following expression:

$$V_{o1} = \frac{2V_m}{\pi} \cos \varphi \quad (12)$$

From (12), it can be seen that output of the integrator contains both amplitude and phase information of the input signal. In this paper, the channel output is obtained by the voltage difference between the integral value of Capacitor 1 and that of Capacitor 2:

$$V_{ch1} = V_{o1} - V_{o2} = \frac{4V_m}{\pi} \cos \varphi \quad (13)$$

Similar to the above derivation, to obtain the amplitude and phase of input signal easily, it just needs to add another switch control signal that is orthogonal to the current signal in channel 1. The integral output of channel 2 can be written as:

$$V_{ch2} = \frac{4V_m}{\pi} \sin \varphi \quad (14)$$

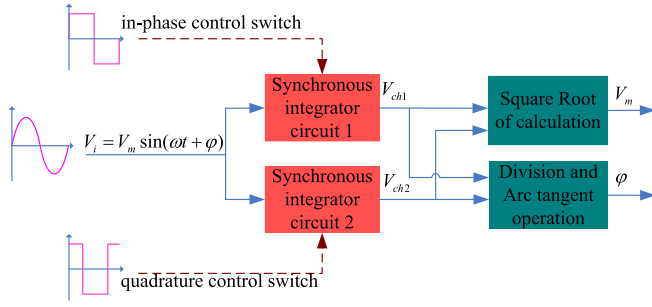


Fig. 4. The flow diagram of synchronous integrator demodulation circuit.

The amplitude and phase information of input signal, therefore, can be obtained as:

$$\begin{cases} V_m = \frac{\pi}{4} \sqrt{V_{ch1}^2 + V_{ch2}^2} \\ \varphi = \arctg\left(\frac{V_{ch2}}{V_{ch1}}\right) \end{cases} \quad (15)$$

Hence, the synchronous integrator can be considered as a quadrature demodulator. The flow diagram, as shown in Fig. 4, demonstrates the demodulation procedure that obtains the amplitude and phase of the input signal.

#### IV. FREQUENCY CHARACTERISTIC ANALYSIS OF SYNCHRONOUS INTEGRATOR

The above analysis is based on the assumption that the frequencies of the input signal and the reference signal are identical, i.e.,  $\omega = \omega_R = \omega_d$ , which is suitable for drive mode and sense mode of gyroscope in a stationary state. When the input angular rate  $\Omega_z$  is applied to the gyroscope, we define the input angular rate as:

$$\Omega_z = \Omega \sin(\omega_z t) \quad (16)$$

where  $\Omega$  is the amplitude and  $\omega_z$  is the frequency of the input angular rate. According to the Coriolis effect, the Coriolis force can be represented as:

$$\begin{aligned} F_c(t) &= -2m_y \Omega_z(t) \dot{x}(t) \\ &= -m_y \Omega A_x \omega_d [\cos((\omega_d + \omega_z)t) - \cos((\omega_d - \omega_z)t)] \end{aligned} \quad (17)$$

From (17), it can be observed that the Coriolis signal is a modulated signal, whose frequency is different from the reference signal, containing the frequencies of  $\omega_d \pm \omega_z$ .

Hence, it is necessary to research the frequency characteristic of the synchronous integrator, which has impact on the bandwidth of gyroscope. Assume the frequency of input signal is  $\omega = \omega_d + \omega_z = \omega_R + \Delta\omega$ , where  $\Delta\omega$  is the deviation value of the input signal and the reference signal. Substituting  $\omega = \omega_R + \Delta\omega$  into (8) yields:

$$\begin{aligned} V_{o1}(\Delta\omega) &= \frac{2V_m}{\pi} \left( \frac{\cos(\Delta\omega \cdot t + \varphi + \theta_1)}{\sqrt{1 + (2RC_1 \Delta\omega)^2}} \right. \\ &\quad \left. - e^{-\frac{t}{2RC_1}} \frac{\cos(\varphi + \theta_1)}{\sqrt{1 + (2RC_1 \Delta\omega)^2}} \right) \end{aligned} \quad (18)$$

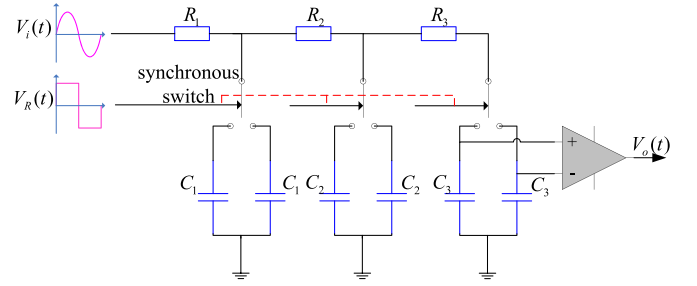


Fig. 5. The third-order synchronous integrator circuit.

Considering  $t \gg 2RC$ , it can be simplified as:

$$\hat{V}_{o1}(\Delta\omega) = \frac{2V_m}{\pi} \cdot \frac{\cos(\Delta\omega \cdot t + \varphi + \theta_1)}{\sqrt{1 + (2RC_1 \Delta\omega)^2}} \quad (19)$$

Comparing (19) with (12), it can be found that the output amplitude of synchronous integrator depends on  $\Delta\omega$  with the relationship of  $1/\sqrt{1 + (2RC_1 \Delta\omega)^2}$ , which is same as a first-order RC low-pass filter with the cutoff frequency of  $\omega_c = 1/(2RC_1)$ . As  $\Delta\omega$  can be positive or negative, the synchronous integrator can be regarded as a band-pass filter whose central frequency is the reference frequency. The bandwidth of the synchronous integrator is determined by the time constant  $RC$ , also known as integration time. When the integration time is larger, the pass band is narrower.

In this paper, the synchronous integrator circuit is shown in fig. 5. It uses a third-order cascaded form where the first-order synchronous integrator has been theoretically analyzed in Section III.

From the analysis in Section III, the output voltage of the first-order synchronous integrator is  $V_{o1}$  whose amplitude can be written as follows:

$$\hat{V}_{o1}(\Delta\omega) = \frac{2V_m}{\pi} \cdot \frac{\cos(\Delta\omega \cdot t + \varphi + \theta_1)}{\sqrt{1 + (2R_1 C_1 \Delta\omega)^2}} \quad (20)$$

where  $R_1$  is the value of resistor and  $C_1$  is the value of capacitor of the first-order synchronous integrator. Substituting  $\omega = \omega_R + \Delta\omega$  into (9) gives:

$$\theta_1(\Delta\omega) = \arctg(2R_1 C_1 \Delta\omega) \quad (21)$$

The output voltage of the first-order synchronous integrator is regarded as the input of the second-order. In general, under the condition of  $R_1 = R_2 = R_3 = R$  and  $C_1 = C_2 = C_3 = C$ , transfer function of the third-order cascade synchronous integrator is similar to the third-order RC low-pass filter as follows:

$$\begin{aligned} H(s) &= \frac{V_o(s)}{V_i(s)} \\ &= \frac{2V_m}{\pi} \cdot \frac{1}{(2RCs)^3 + 5 \cdot (2RCs)^2 + 6 \cdot (2RCs) + 1} \end{aligned} \quad (22)$$

The output of the third-order cascaded synchronous integrator in the time domain can be expressed as:

$$\begin{aligned} V_o(\Delta\omega) &= \frac{2V_m}{\pi} \cdot \frac{1}{\sqrt{[12RC\Delta\omega - (2RC\Delta\omega)^3]^2 + [1 - 5 \cdot (2RC\Delta\omega)^2]^2}} \\ &\quad \cdot \cos(\Delta\omega \cdot t + \varphi + \theta') \end{aligned} \quad (23)$$

Let  $\omega_0 = 1/(2RC)$ , the expression of amplitude-frequency can be written as follows:

$$\begin{cases} A_1(\Delta\omega) = \frac{2V_m}{\pi} \cdot \frac{1}{\sqrt{(\Delta\omega/\omega_0)^2 + 1}} \\ A_2(\Delta\omega) = \frac{2V_m}{\pi} \cdot \frac{1}{\sqrt{(\Delta\omega/\omega_0)^6 + 13 \cdot (\Delta\omega/\omega_0)^4 + 26 \cdot (\Delta\omega/\omega_0)^2 + 1}} \end{cases} \quad (24)$$

where  $A_1(\Delta\omega)$  is the expression of amplitude-frequency of a first-order synchronous integrator;  $A_2(\Delta\omega)$  is the expression of amplitude-frequency of a third-order cascaded synchronous integrator, whose cutoff frequency can be deduced as:

$$\Delta\omega_c = 0.19428 \cdot \omega_0 = 0.19428/(2RC) \quad (25)$$

We can set up the bandwidth of the third-order cascaded synchronous integrator based on (25).

Transforming (24) to Logarithmic form, it can be written as:

$$\begin{cases} L_1(\Delta\omega) = 20 \lg |A_1(\Delta\omega)| \\ \quad = -10 \lg((\Delta\omega/\omega_0)^2 + 1) + 20 \lg(\frac{2V_m}{\pi}) \\ \quad \approx -20 \lg(\Delta\omega/\omega_0) + 20 \lg(\frac{2V_m}{\pi}) \\ L_2(\Delta\omega) = 20 \lg |A_2(\Delta\omega)| \\ \quad = -10 \lg[(\Delta\omega/\omega_0)^6 + 13 \cdot (\Delta\omega/\omega_0)^4 \\ \quad \quad + 26 \cdot (\Delta\omega/\omega_0)^2 + 1] + 20 \lg(\frac{2V_m}{\pi}) \\ \quad \approx -60 \lg(\Delta\omega/\omega_0) + 20 \lg(\frac{2V_m}{\pi}) \end{cases} \quad (26)$$

From (26), it can be seen that the gain of first-order synchronous integrator is reduced as 20 db/dec and the gain of third-order cascaded synchronous integrator is reduced approximately as 60 db/dec. It shows that the ability of suppressing interference for the cascaded synchronous integrator is the sum of ability of each order.

From (23), when the frequencies of input signal and reference signal are equal, i.e.,  $\Delta\omega = 0$ , it can be deduced as:

$$V_0 = \frac{2V_m}{\pi} \cos \varphi \quad (27)$$

Equation (27) has the same form of (12). When the frequencies of input signal and reference signal are the same, the output of cascaded synchronous integrator does not attenuate and its ability to suppress noise is better than that of the first-order synchronous integrator.

Therefore, the control system of gyroscope adopts a third-order cascaded synchronous integrator circuit instead of a first-order synchronous integrator circuit to demodulate the signals of drive mode and sense mode.

Due to the bandwidth requirement of gyroscope, the bandwidth of the demodulation circuit must be wider than that of gyroscope in working. Equation (5) has showed the bandwidth of gyroscope when it works in open-loop mode.

## V. SIMULATIONS AND COMPARISONS

In this section, simulation systems are built using Simulink to investigate the performance of the Synchronous Integral

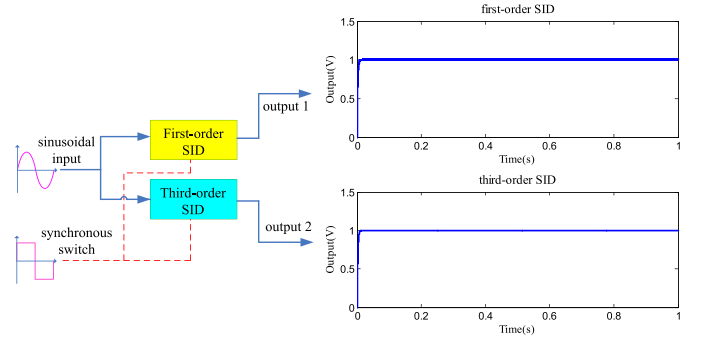


Fig. 6. The output of the first-order SID and the third-order SID. The input signal is a sinusoidal wave with the frequency of 4 KHz and the amplitude of 1 V. The synchronous switch is a square wave with the frequency of 4 kHz and the amplitude of 1 V.

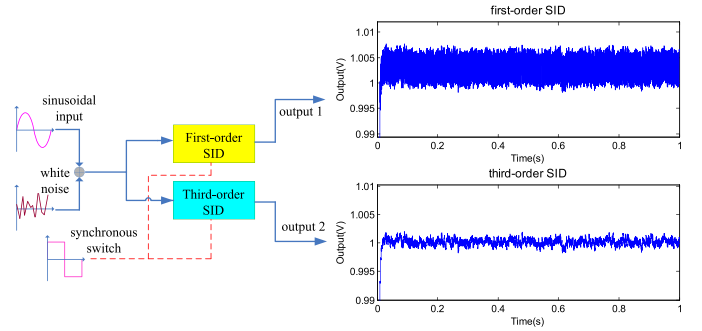


Fig. 7. The anti-noise performance of the first-order SID and the third-order SID. The input signal is a sinusoidal wave of 1V superposed by a white noise with standard deviation of 0.01V. The synchronous switch is a square wave with the frequency of 4 kHz and the amplitude of 1 V.

Demodulator (SID) and compare four demodulator algorithms, including Multiplication Demodulator (MD), Least Mean Square Demodulator (LMSD), Fourier series Demodulator (FD) and Synchronous Integral Demodulator (SID).

### A. The Simulation Verification of the SID

Fig.6 shows the output of a first-order SID and a third-order SID provided that the frequency of input signal and reference signal are the same. It can be found that the output amplitude of third-order SID is equal to the first-order SID, which verifies the output of the cascaded synchronous integrator does not attenuate when the frequencies of input signal and reference signal are the same.

Fig.7 shows the anti-noise performances of the first-order SID and the third-order SID. The input signal is a sinusoidal wave of 1V superposed by a white noise with standard deviation of 0.01V. It can be seen that the third-order synchronous integrator circuit's ability to suppress noise is better than that of the first-order synchronous integrator.

In order to verify the frequency characteristic of the third-order SID, the input signal  $V_z$  is modulated on a 4 kHz sinusoidal signal  $V_d$  and then fed to the third-order SID. Fig.8(a) illustrates the input-output curve plotted by the third-order synchronous integrator circuit. The bode diagram is shown in fig. 8(b) based on the system transfer function of the third-order SID as given in (22). We can find that the



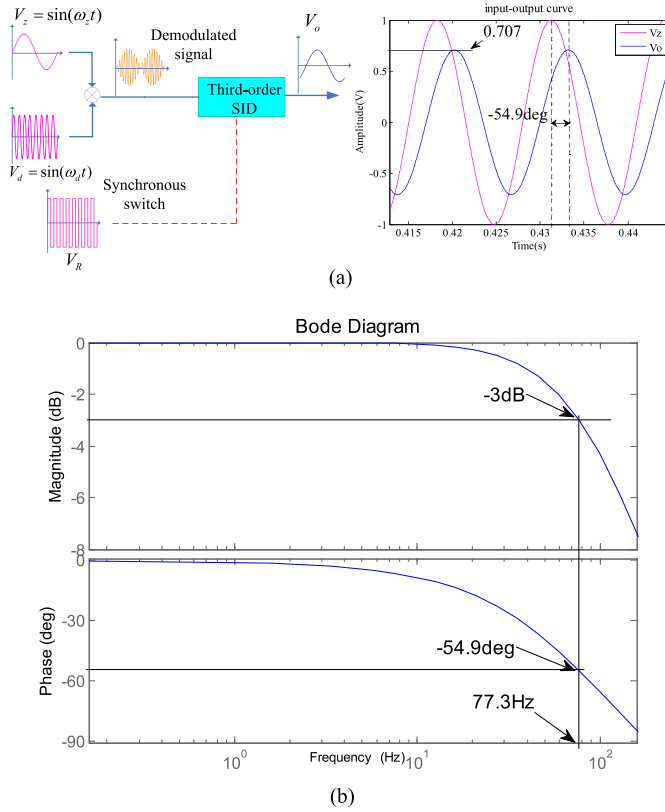


Fig. 8.  $R = 10 \text{ k}\Omega$ ,  $C = 20 \text{ nF}$ . (a) The input-output curve of the third-order SID circuit.  $\omega_z = 2\pi \cdot 77.3 \text{ (rad)}$ ,  $\omega_d = \omega_R = 2\pi \cdot 4000 \text{ (rad)}$ . (b) The bode diagram of the third-order SID.

bandwidth of the third-order SID is 77.3 Hz with the parameter of 10 k $\Omega$  resistance and 20 nF capacitance, and the phase of  $V_o$  lags 54.9 degrees with respect to that of  $V_z$ .

### B. Comparisons of Simulations for Several Demodulation Algorithms

The four demodulation algorithms, including MD, LMSD, FD and SID, are simulated by MATLAB to compare their performances.

The input signal is a sinusoidal wave with the amplitude of 1 V and the frequency of 4 kHz superposed with a Gauss white noise whose mean value is 0 V and standard deviation 0.1 V. In order to compare the performances of these algorithms fairly, it is necessary to guarantee the same bandwidth of the four demodulation algorithms. Set the demodulation bandwidth as 75 Hz, therefore, MD includes one two-order low-pass filter with cutoff frequency of 75 Hz, convergence factor of LMSD is 0.0073, the value of resistor and capacitor of SID are 10 k $\Omega$  and 20 nF, and each demodulated output of FD is obtained by eight signal period with the sampling frequency of 64 kHz.

Fig. 9(a) and (b) show the startup time and power spectral density of four demodulation algorithms, respectively. From the simulation results shown in these two figures, we can find that the difference in the startup time is quite small and the FD algorithm has a shorter startup time. SID has the lowest noise level and a better ability to attenuate the harmonics.

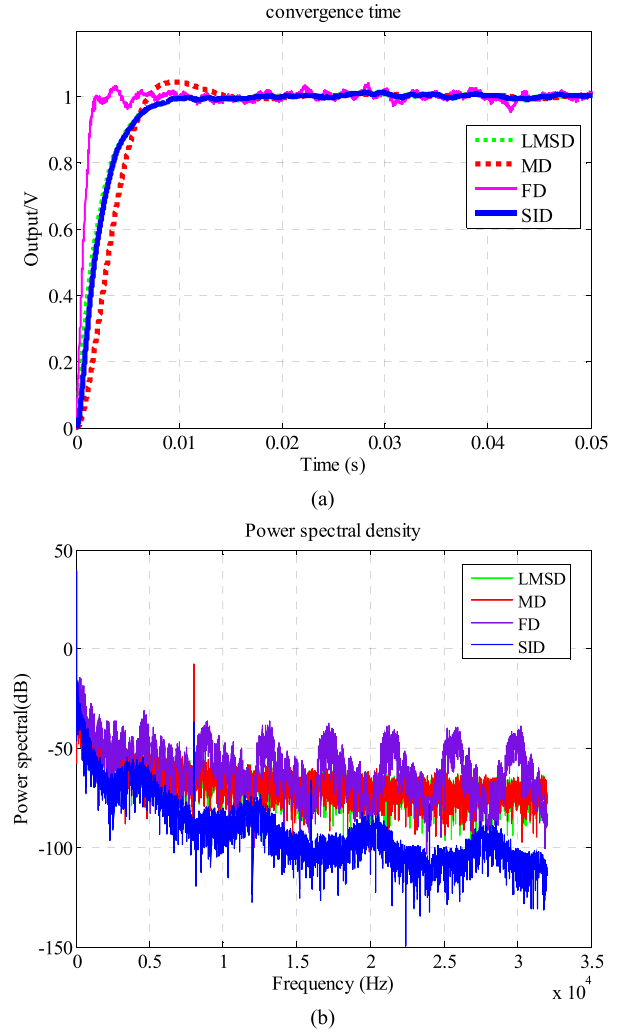


Fig. 9. (a) The startup time of four demodulation algorithms. (b) The noise level of four demodulation algorithms.

TABLE I  
COMPARISON OF THE FOUR DEMODULATION ALGORITHMS

DEMOMULATION ALGORITHM	STARTUP TIME	NOISE LEVEL	HARDWARE LOGIC ELEMENTS
MD	15ms	-70dB	234
LMSD	10ms	-70dB	386
FD	5ms	-60dB	3166
SID	10ms	-100dB	125

According to the occupied digital hardware resources listed in Table I, the SID algorithm has the highest hardware efficiency.

Making trade-offs between the startup speed, noise and hardware resource realized in FPGA, the SID algorithm is selected in our system.

## VI. THE CONTROL SYSTEM OF MEMS TUNING FORK GYROSCOPE

This paper introduces a novel demodulation algorithm, synchronous integrator demodulation algorithm, demodulating the drive-detection signal and the sensitive-axis detection signal

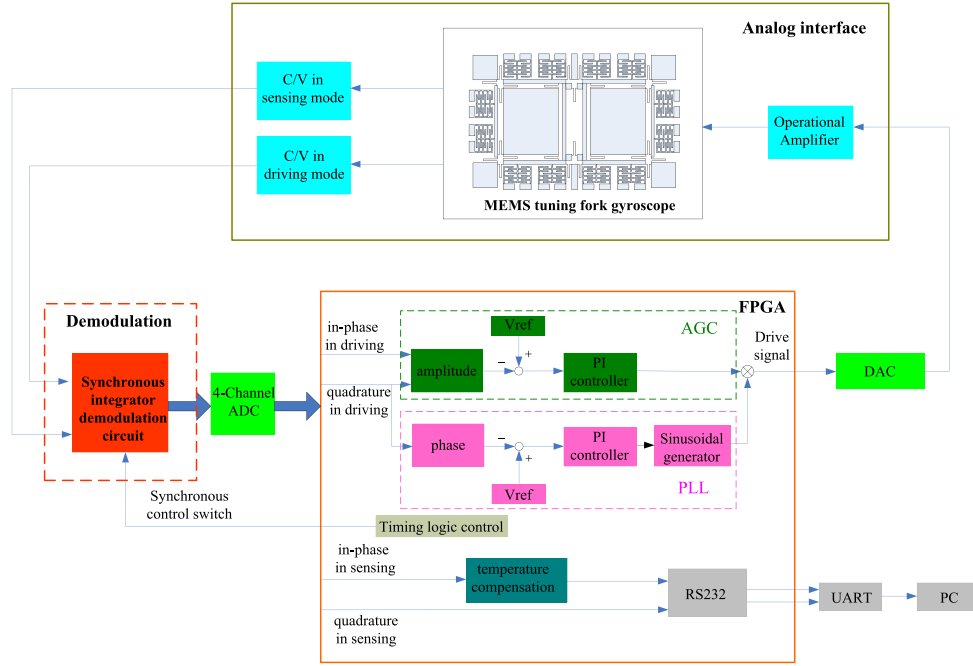


Fig. 10. The digital control system of the MEMS tuning fork gyroscope.

respectively. The MEMS tuning fork gyroscope control system is shown in fig. 10. The system consists of three parts, namely, analog interface circuit, synchronous integrator circuit and digital control circuit. Among them, synchronous integrator circuit and digital control circuit are the key parts of the gyroscope control system. Analog interface section includes capacitance/voltage (C/V) conversion circuit and amplifier circuit. The output signals of drive direction and sense direction are controlled separately by two orthogonal switching signals generated by the FPGA. The four-channel demodulated signals are converted into the FPGA to extract the amplitude and phase information. In the drive mode, the amplitude and phase of drive detection signal are used to control the drive loop stably. In order to drive the gyroscope under fixed amplitude and stable phase conditions, the control system introduces automatic gain control (AGC) [20] technology to stabilize amplitude and phase-locked loop (PLL) [21] technology to track phase and frequency. In the sense mode, the SID can obtain Coriolis signal and quadrature-error signal separately. Sense circuit uses the open-loop detection method and adds the temperature compensation module. The angular rate output is displayed on the computer via RS232.

## VII. EXPERIMENTS AND RESULTS

In order to verify the effectiveness of synchronous integrator demodulation algorithm in MEMS tuning fork gyroscope control system, the gyroscope control circuit is designed and relevant tests are carried out. Fig. 11 shows the gyroscope system circuit and experimental test equipment.

The key technology of synchronous integrator circuit is the switch control signal that is generated by the Direct Digital Synthesizer (DDS) technology [22] via FPGA in this gyroscope control system. Using the same frequency control

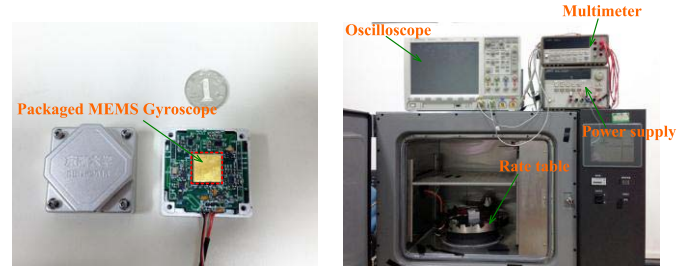


Fig. 11. Circuit of the MEMS tuning fork gyroscope and test equipment.

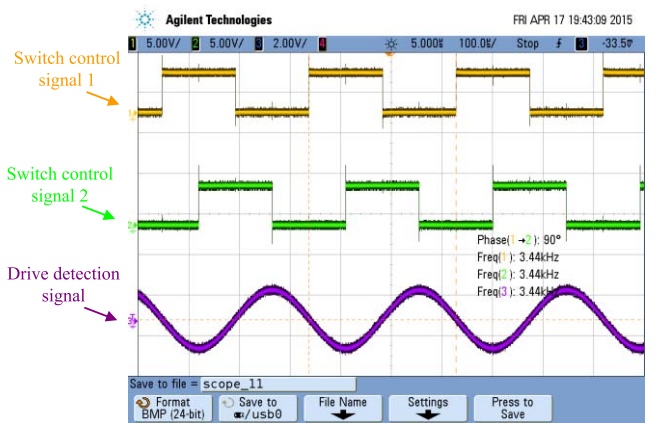


Fig. 12. Switch control signals in Channel 1 and Channel 2. Drive detection signal of the gyroscope is shown in Channel 3. The frequencies of them are all the same with 3438.1 Hz.

word (FCW) ensures the frequency of the switch control signal consistent with that of drive signal of the gyroscope. This avoids the impact of frequency difference between the input and the reference signals [23]. In order to verify the switch control signal of synchronous integrator circuit, two orthogonal switch signals of driving control loop are

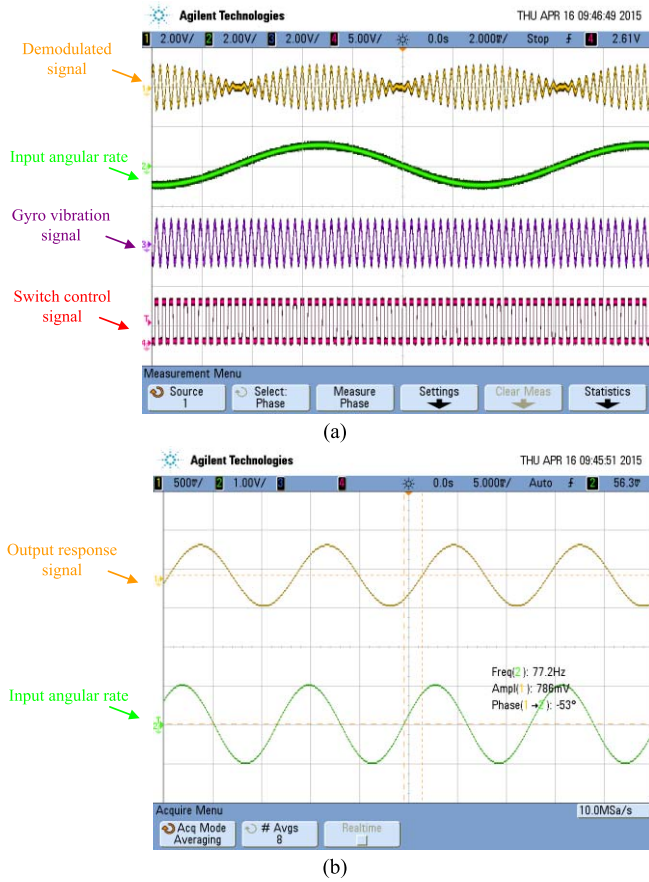


Fig. 13. (a) The four-channel signal generated by FPGA. (b) The input and output relationship revealing the frequency characteristic.

TABLE II

DESIGN PARAMETERS OF THE TESTED MEMS GYROSCOPE

PARAMETER	VALUES
Drive mode natural frequency(f <sub>d</sub> )	3438.1Hz
Drive mode quality factor(Q <sub>d</sub> )	5500
Sense mode natural frequency(f <sub>s</sub> )	3347.9Hz
Sense mode quality factor(Q <sub>s</sub> )	7000
Drive effective mass(m <sub>x</sub> )	$1.42 \times 10^{-6}$ kg
Sense effective mass(m <sub>y</sub> )	$1.58 \times 10^{-6}$ kg
Drive mode capacitance(C <sub>d</sub> )	2.88pF
Sense mode capacitance(C <sub>s</sub> )	4.68pF
Drive mode displacement amplitude(x <sub>d</sub> )	5μm

observed by oscilloscope. Two-channel switch control signals can be seen from fig.12, and the two signals are the strictly orthogonal. Fig.12 also shows that the switch control signal has the same frequency as the drive signal of gyroscope. These provide the necessary conditions for the synchronous integrator demodulation circuit to demodulate the amplitude and phase of gyroscope signal.

In order to verify the dynamic response of the actual synchronous integrator circuit applied to the gyroscope system. Similar to the fig.8(a), we used FPGA to generate the demodulated signal (Channel 1), the input angular rate signal (Channel 2), the gyro vibration signal (Channel 3) and switch

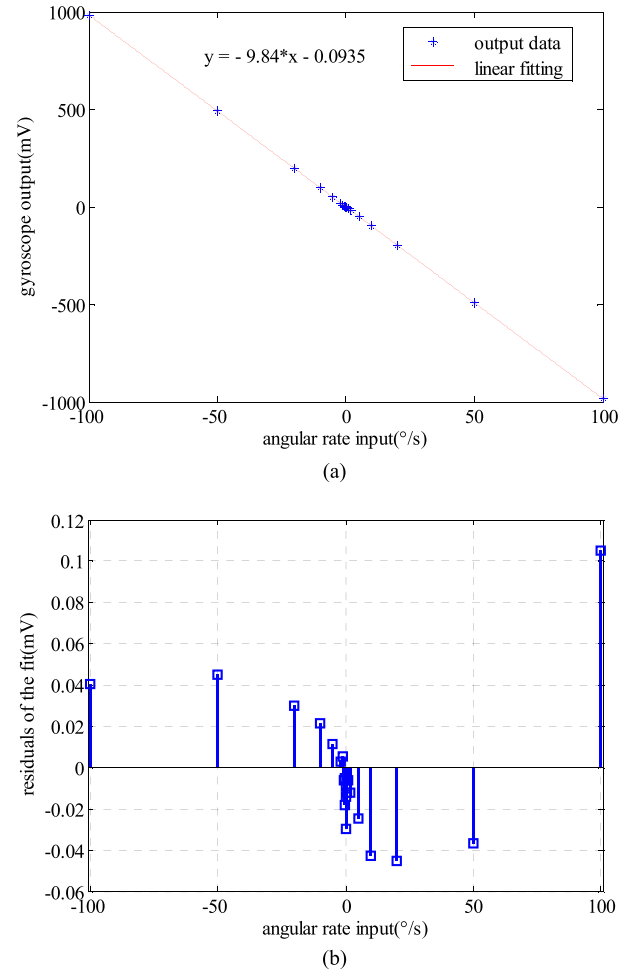


Fig. 14. (a) Scale factor of the tested gyroscope. (b) Residual error between the measured data and fitting data.

TABLE III

TESTING RESULT OF THE TESTED GYROSCOPE

PARAMETER	VALUES
Bias instability(Allan variance)	0.2°/h
Angular random walk(ARW)	0.14°/√h
Scale factor	9.84mV /°/s
Scale factor's nonlinearity	60ppm
Measurement range	±100°/s
Bandwidth	47Hz
Supply	±8V
Power consumption of ADC	30mW
Power consumption of FPGA	300mW
Power consumption of DAC	20mW
Power consumption of the analog interface	150mW

control signal (Channel 4). The demodulated signal is fed to the synchronous integrator circuit. Fig.13(a) shows these four-channel signals and fig. 13(b) shows the input and output relationship revealing the frequency characteristic, which is consistent with the simulation in Section V.

In order to test the overall performance of the gyroscope control system under normal operating conditions, the system



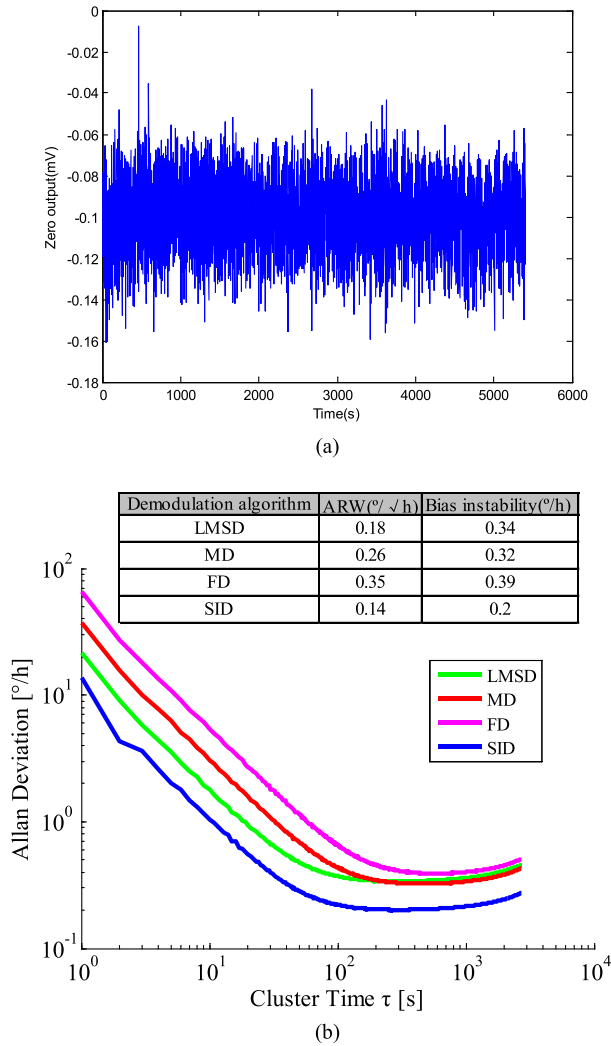


Fig. 15. (a) Zero-rate output of the tested gyroscope. (b) The Allan variance graphic of the tested gyroscope by using different demodulation algorithms.

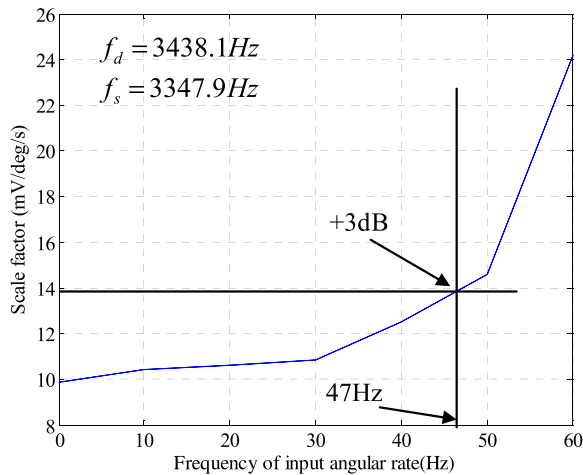


Fig. 16. The bandwidth test of the gyroscope, whose frequencies of drive mode and sense mode are 3438.1 Hz and 3347.9 Hz, respectively.

works continuously in the temperature control oven and the rate table. The design parameters of the tested MEMS tuning fork gyroscope are summarized in Table II. For open-loop mode, the rms rate equivalent noise (REN) of the gyroscope operated in mode-mismatched is given by [24], the minimum

detectable rate can be calculated as the order of  $0.05^\circ/\text{h}$ . Fig. 14(a) shows the scale factor of gyroscope at room temperature and fig. 14(b) shows the residuals of the fit. When the input angular rate is  $100^\circ/\text{s}$ , the residual error between the measured data and fitting data reaches to maximum. With the scale factor of  $9.84\text{mV}/^\circ/\text{s}$  in full-scale range of  $\pm 100^\circ/\text{s}$ , the nonlinearity is less than 60 ppm. The zero-rate output (ZRO) data were collected for the Allan variance analysis by using MD, LMSD, FD and SID algorithms, respectively. Fig. 15(a) shows the zero-rate output (ZRO) of the tested gyroscope by using SID and the Allan variance graphic is plotted in fig. 15(b). The bias instability and angle random walk obtained by different demodulation algorithms are also list in fig. 15(b). The Allan variance graphic shows the best performance of  $0.2^\circ/\text{h}$  bias instability and  $0.14^\circ/\sqrt{\text{h}}$  ARW with SID.

The dynamic response of the gyroscope is tested as shown in fig. 16. The bandwidth of the gyroscope is about 47Hz, in close agreement with the (5). It is based on the frequency difference between the drive mode and sense mode and not affected by the synchronous integrator circuit. The testing results are listed in Table III.

## VIII. CONCLUSION

The precision of MEMS gyroscope is quite lower than those of traditional gyroscopes. Researching novel circuit technologies and control algorithms are the effective ways to further improve the performance of micro-gyroscope. In this paper, the synchronous integral demodulator (SID) applied in the gyroscope digital control system is analyzed and studied in detail.

Synchronous integrator circuit is the effective means to detect weak signals from noise, having strong anti-noise properties. This paper introduces the circuit as the quadrature demodulator to obtain the amplitude and phase information of demodulated signal by the orthogonal switch control signals. The simulation results have verified the effectiveness of the SID, which is in good agreement with the theoretical analysis. Compared with other demodulation algorithms, the SID has the advantages of the lower noise level, a better ability to attenuate the harmonics and the highest hardware efficiency.

Combing with AGC and PLL technology, the closed-loop control of drive mode and high precision output of sense mode of MEMS tuning fork gyroscope developed in our laboratory have been implemented. The zero bias instability of tested gyroscope has achieved  $0.2^\circ/\text{h}$  and the nonlinearity of scale factor is less than 60 ppm. Contribution to fewer FPGA logic resources, the scheme requires lower power consumption, and the control algorithm is relatively simple.

Consequently, the scheme of synchronous integral demodulator for MEMS tuning fork gyroscope is effective and reliable.

## REFERENCES

- [1] D. K. Shaeffer, "MEMS inertial sensors: A tutorial overview," *IEEE Commun. Mag.*, vol. 51, no. 4, pp. 100–109, Apr. 2013.
- [2] W. Geiger *et al.*, "MEMS IMU for AHRS applications," in *Proc. IEEE/ION Position, Location Navigat. Symp.*, vol. 1, May 2008, pp. 225–231.

- [3] R. Maimon, O. Lahav, Y. Gerson, O. Zohar, H. Berko, and S. Krylov, "Tactical grade micro gyroscope with dual capacitive/optical sensing," in *Proc. IEEE 26th Int. Conf. Micro Electro Mech. Syst. (MEMS)*, Jan. 2013, pp. 637–640.
- [4] I. P. Prikhodko, S. A. Zotov, A. A. Trusov, and A. M. Shkel, "What is MEMS gyrocompassing? Comparative analysis of maytagging and carouseling," *J. Microelectromech. Syst.*, vol. 22, no. 6, pp. 1257–1266, Dec. 2013.
- [5] I. P. Prikhodko, S. A. Zotov, A. A. Trusov, and A. M. Shkel, "Sub-degree-per-hour silicon MEMS rate sensor with 1 million Q-factor," in *Proc. 16th Solid-State Sens., Actuators, Microsyst. Conf.*, Jun. 2011, pp. 2809–2812.
- [6] B. Chaumet, B. Leverrier, C. Rougeot, and S. Bouyat, "A new silicon tuning fork gyroscope for aerospace applications," in *Proc. Symp. Gyro Technol.*, Sep. 2009, pp. 1.1–1.13.
- [7] M. Saukoski, L. Aaltonen, and K. A. I. Halonen, "Zero-rate output and quadrature compensation in vibratory MEMS gyroscopes," *IEEE Sensors J.*, vol. 7, no. 12, pp. 1639–1652, Dec. 2007.
- [8] J. Raman, E. Cretu, P. Rombouts, and L. Weyten, "A closed-loop digitally controlled MEMS gyroscope with unconstrained sigma-delta force-feedback," *IEEE Sensors J.*, vol. 9, no. 3, pp. 297–305, Mar. 2009.
- [9] D. Xia, C. Yu, and Y. L. Wang, "A digitalized silicon microgyroscope based on embedded FPGA," *Sensors*, vol. 12, no. 10, pp. 13150–13166, Sep. 2012.
- [10] A. Norouzpour-Shirazi, M. F. Zaman, and F. Ayazi, "A digital phase demodulation technique for resonant MEMS gyroscopes," *IEEE Sensors J.*, vol. 14, no. 9, pp. 3260–3266, Sep. 2014.
- [11] M. Saukoski, L. Aaltonen, and K. A. I. Halonen, "Effects of synchronous demodulation in vibratory MEMS gyroscopes: A theoretical study," *IEEE Sensors J.*, vol. 8, no. 10, pp. 1722–1733, Oct. 2008.
- [12] N. Lu *et al.*, "An FPGA implementation of the LMS adaptive filter for MEMS gyroscope," in *Proc. 5th IEEE Int. Conf. Nano/Micro Eng. Molecular Syst.*, Jan. 2010, pp. 744–747.
- [13] D. Xia, C. Yu, and L. Kong, "The development of micromachined gyroscope structure and circuitry technology," *Sensors*, vol. 14, no. 1, pp. 1394–1473, Jan. 2014.
- [14] D. Liu, C. He, Q. Zhao, Z. Yang, Y. Hao, and G. Yan, "Digital signal processing for a micromachined vibratory gyroscope based on a three dimensional adaptive filter demodulator," *Measurement*, vol. 50, pp. 198–202, Apr. 2014.
- [15] C. Yang, H. S. Li, J. Y. Chen, and X. L. Wang, "Design and test of silicon Micromachined gyroscope control system based on Fourier demodulation algorithm," *J. Southeast Univ. (Natural Sci. Ed.)*, vol. 44, no. 3, pp. 550–555, May 2014.
- [16] R. H. Frater, "Synchronous integrator and demodulator," *Rev. Sci. Instrum.*, vol. 36, no. 5, pp. 634–637, May 1965.
- [17] H. Cao and H. Li, "Investigation of a vacuum packaged MEMS gyroscope architecture's temperature robustness," *Int. J. Appl. Electromagn. Mech.*, vol. 41, no. 4, pp. 495–506, 2013.
- [18] H. Cao, H. Li, X. Sheng, S. Wang, B. Yang, and L. Huang, "A novel temperature compensation method for a MEMS gyroscope oriented on a periphery circuit," *Int. J. Adv. Robot. Syst.*, vol. 10, pp. 1–10, Jul. 2013.
- [19] Y. Ni, H. Li, L. Huang, X. Ding, and H. Wang, "On bandwidth characteristics of tuning fork micro-gyroscope with mechanically coupled sense mode," *Sensors*, vol. 14, no. 7, pp. 13024–13045, Jul. 2014.
- [20] S. E. Alper, K. Sahin, and T. Akin, "An analysis to improve stability of drive-mode oscillations in capacitive vibratory MEMS gyroscopes," in *Proc. 22nd IEEE Int. Conf. Micro Electro Mech. Syst.*, Jan. 2009, pp. 817–820.
- [21] M. Saukoski, L. Aaltonen, T. Salo, and K. A. I. Halonen, "Interface and control electronics for a bulk micromachined capacitive gyroscope," *Sens. Actuators A, Phys.*, vol. 147, no. 1, pp. 183–193, 2008.
- [22] H. Omran, K. Sharaf, and M. Ibrahim, "An all-digital direct digital synthesizer fully implemented on FPGA," in *Proc. 4th IEEE Int. Conf. Design Test Workshop (IDT)*, Nov. 2009, pp. 1–6.
- [23] H. Zhu, J. Lin, Z. H. Wang, and X. X. Zhan, "Design and application of the lock-in amplifier automatically adjusting the frequency of reference signal," *Chin. J. Sci. Instrum.*, vol. 25, no. 4, pp. 66–68, Aug. 2004.
- [24] R. P. Leland, "Mechanical-thermal noise in MEMS gyroscopes," *IEEE Sensors J.*, vol. 5, no. 3, pp. 493–500, Jun. 2005.

**Cheng Yang** received the B.S. degree in control technology and instrument from Southeast University, Nanjing, China, in 2011, where he is currently pursuing the Ph.D. degree with the Key Laboratory of Microinertial Instrument and Advanced Navigation Technology, Ministry of Education.

His current research interests include the MEMS inertial sensor and circuit design.

**Hongsheng Li** received the B.S. degree in automatic control engineering and the Ph.D. degree from the Department of Instrument Science and Engineering, Southeast University, Nanjing, China, in 1984 and 1994, respectively.

He was a Post-Doctoral Fellow with the Huazhong University of Science and Technology, from 1995 to 1997. He is currently a Professor with the School of Instrument Science and Engineering and the Director with the Institute of Microinertial Systems and Devices, Southeast University. His current research interests include the MEMS inertial sensor, weak signal process, and circuit design.